



## Article

# Phosphorus-Rich Ruthenium Phosphide Embedded on a 3D Porous Dual-Doped Graphitic Carbon for Hydrogen Evolution Reaction

Aicha Anouar <sup>1,2,\*</sup> , Antonio Doménech-Carbó <sup>3,\*</sup> and Hermenegildo Garcia <sup>2,\*</sup>

<sup>1</sup> Engineering Division, Euromed Research Institute, EuroMed University of Fes (UEMF), Route de Meknes, Rond-Point de Bensouda, Fès 30070, Morocco

<sup>2</sup> Departamento de Química (UPV), Instituto de Tecnología Química (CSIC-UPV), Universitat Politècnica de València, Av. de los Naranjos s/n, 46022 Valencia, Spain

<sup>3</sup> Departament de Química Analítica, Universitat de València, Dr. Moliner 50, Burjassot, 46100 Valencia, Spain

\* Correspondence: a.anouar@ueuromed.org (A.A.); antonio.domenech@uv.es (A.D.-C.); hgarcia@qim.upv.es (H.G.)

**Abstract:** Metal phosphides have recently emerged as promising electrocatalysts for hydrogen evolution reaction (HER). Herein, we report the synthesis of ruthenium diphosphide embedded on a dual-doped graphitic carbon by pyrolyzing chitosan beads impregnated with ruthenium chloride and phosphorus pentoxide. The as-synthesized RuP<sub>2</sub>@N-P-C displays a good electrocatalytic activity in acidic, neutral and alkaline media. We show that the HER activity of the electrocatalyst can be tuned by varying the concentration of Li<sup>+</sup> cations. Co-diffusion effects on H<sup>+</sup> exerted by Li<sup>+</sup> on HER in the porous carbon matrix have been observed.

**Keywords:** ruthenium electrocatalysts; metal phosphides; ruthenium diphosphide; dual-doped graphitic carbon; hydrogen evolution reaction



**Citation:** Anouar, A.;

Doménech-Carbó, A.; Garcia, H.

Phosphorus-Rich Ruthenium

Phosphide Embedded on a 3D

Porous Dual-Doped Graphitic

Carbon for Hydrogen Evolution

Reaction. *Nanomaterials* **2022**, *12*, 3597.

[https://doi.org/10.3390/](https://doi.org/10.3390/nano12203597)

[nano12203597](https://doi.org/10.3390/nano12203597)

Academic Editor: Genqiang Zhang

Received: 19 September 2022

Accepted: 10 October 2022

Published: 13 October 2022

**Publisher's Note:** MDPI stays neutral with regard to jurisdictional claims in published maps and institutional affiliations.



**Copyright:** © 2022 by the authors.

Licensee MDPI, Basel, Switzerland.

This article is an open access article

distributed under the terms and

conditions of the Creative Commons

Attribution (CC BY) license ([https://creativecommons.org/licenses/by/](https://creativecommons.org/licenses/by/4.0/)

[https://creativecommons.org/licenses/by/](https://creativecommons.org/licenses/by/4.0/)

[4.0/](https://creativecommons.org/licenses/by/4.0/)).

## 1. Introduction

With the exhaustion of fossil fuels and ongoing global warming, referring to clean and sustainable energy resources is of paramount importance [1,2]. Hydrogen (H<sub>2</sub>), a carbon-free and clean energy is regarded as an attractive energy vector for transportation and for the chemical storage of green electricity [3,4]. The current production of hydrogen by steam reforming of natural gas consumes fossil fuels and emits equivalent amounts of carbon dioxide (CO<sub>2</sub>) contributing to the greenhouse effect [5,6]. Implementation of the industrial, large scale hydrogen production by electrocatalytic water splitting with renewable electricity is set to overcome these issues as it is a carbon-zero process allowing for the production of green hydrogen [7].

To this date, Pt-based electrocatalysts constitute the most active catalysts for hydrogen evolution reaction (HER) [8]. Unfortunately, however, the towering cost and scarcity of this element is one of the bottlenecks limiting the massive production of green hydrogen [9]. Most of the studies focusing on the remarkable activity of Pt are carried out in acidic media, yet Pt-based electrocatalysts display about two orders of magnitude lowered activity in alkaline media due to sluggish kinetics [10]. Ruthenium (Ru), a relatively cheaper metal has demonstrated respectable activity in HER with minute overpotentials and extremely low on-set potentials [11–13] ascribed to similar metal-hydrogen bonding to that of Pt and decreased water activation barrier [14]. To boost the HER activity, a modulation of the adsorption of reaction intermediates (hydrogen) to the active sites of the electrocatalysts is necessary. For Ru-based electrocatalysts, a strong adsorption of H on Ru surface is generally observed leading to a poor HER activity [15].

As a new class of materials, metal phosphides (MPs) have recently attracted great attention as electrocatalysts for HER and organic molecule electro-oxidation reactions due

to their low cost and high activities [16–18]. Depending on the phosphorus content, MPs exhibit different activities in HER [19]. Compared to metal (M) rich MPs, phosphorus-rich MPs possess lower conductivities due to abundant P-P bonds and M-P bonds and lower density of M-M bonds [19]. Accordingly, RuP nanoparticles demonstrated superior electrocatalytic activity compared to RuP<sub>2</sub> due to the abundance of electrocatalytic active sites and better conductivity [20]. One of the means to enhance the conductivity of P-rich MPs is to support them on carbon materials such as graphene and activated carbons [21]. The support generally exposes more active sites and boosts the electrical conductivity facilitating electron transfer [22]. Most of the strategies used for the synthesis of RuP<sub>x</sub> supported on carbon matrices rely on the use of phosphines, or sodium hypophosphite and are generally not straightforward since several steps are needed to carry out phosphorization [23,24].

Biopolymers such as chitosan (CS) and sodium alginate have the ability to be shaped into three dimensional nanofibrillated microspheres thanks to their pH switchable solubility [25]. The hydrogels resulting from precipitation of these biopolymers in alkaline (CS) or acidic (alginic acid) aqueous solutions, when dehydrated with ethanol, can be dried using CO<sub>2</sub> supercritical conditions and thus allow the obtainment of aerogels with a large surface area and open macroporous network [26]. Pyrolysis of aerogels has been greatly explored to prepare porous graphitic catalysts with intrinsic defects [27–29] on which metallic nanoparticles are grown in situ. Since CS and alginic acid based microspheres have excellent abilities to adsorb phosphates [30,31], P-doped or N,P-dual doped porous graphitic carbon could be easily synthesized through pyrolysis of biopolymers on which phosphates are adsorbed or grafted [21,32].

Recently, a phosphate ester obtained from dissolution of phosphorus pentoxide (P<sub>2</sub>O<sub>5</sub>) in methanol was revealed as an excellent precursor to prepare noncovalent phosphorylated graphene oxide and the resulting material displayed improved hole transport in polymer solar cells [33]. Inspired by this approach, we used P<sub>2</sub>O<sub>5</sub> dissolved in ethanol as P source to grow MPs in situ during pyrolysis of metal containing CS microspheres. The strategy herein reported allows the synthesis of RuP<sub>2</sub> nanoparticles supported in highly porous N,P-codoped graphitic carbon (RuP<sub>2</sub>@N-P-C). The electrocatalytic effect exerted by RuP<sub>2</sub> nanoparticles embedded in nitrogen and phosphorus dual doped graphitic carbon on the hydrogen evolution reaction (HER) was studied at acidic, basic and neutral pHs using usual protocols [34–37]. In acidic media, the catalytic effect of RuP<sub>2</sub>@N-P-C was significantly increased in the presence of Li<sup>+</sup> ions in the electrolyte. This effect, also known in literature, but of unclear explanation [38–40], is studied here focusing the attention on co-diffusion H<sup>+</sup>-Li<sup>+</sup> effects based on voltammetric and electrochemical impedance spectroscopy (EIS) data.

## 2. Materials and Methods

### 2.1. Synthesis of RuP<sub>2</sub>@N-P-C

CS MMW (1000 mg; ACROS) was dissolved in 50 mL of 1.25 vol% acetic acid solution. A complete dissolution was obtained after 21 h of stirring at room temperature. CS beads were formed by dropping the solution through a 0.8 mm syringe into 4 M NaOH solution. CS beads were kept in the alkaline solution for 3 h followed by extensive washings until neutral pH. Forty-two g of the hydrogels obtained were then immersed into a 3.7 mM aqueous RuCl<sub>3</sub> solution for 24 h. The Ru-containing alcogels were obtained by exchanging water with ethanol at increasing ethanol/water ratios (10/90; 30/70; 50/50; 70/30; 90/10; and 100% ethanol). Impregnation of Ru containing alcogels with phosphate was carried out by immersing for 24 h the alcogels in a solution of 700 mg of phosphorus pentoxide (P<sub>2</sub>O<sub>5</sub>) dissolved in 100 mL of ethanol. Dry Ru-phosphate CS aerogels were obtained using an automated CO<sub>2</sub> critical point dryer. The aerogels were pyrolyzed under Ar atmosphere at 5 °C/min until reaching a temperature of 900 °C that was maintained for 1 h. A content of Ru and P of 6.73% and 8.93%, respectively was determined by ICP-OES by dispersing 8 mg of RuP<sub>2</sub>@N-P-C in 8 mL of *aqua regia* and heating at 100 °C for 24 h to completely dissolve Ru and P.

## 2.2. Characterization

Chemical elemental analysis of the electrocatalyst was determined by combustion chemical analysis using a CHNS FISONs elemental analyzer. Specific surface area of RuP<sub>2</sub>@N-P-C was determined by N<sub>2</sub> adsorption isotherms using a Micromeritics 2010 instrument. Field Emission Scanning Electron Microscopy (FESEM) images were acquired using a ZEISS ULTRA 55 microscope equipped with an X-ray detector (EDS). Scanning Transmission Electron Microscopy (STEM) images were acquired using a JEOL JEM 2100F Field Emission Transmission Electron Microscope of 200 kV equipped with an X-ray detector. X-Ray diffraction patterns were recorded using a Cubix Pro PANalytical diffractometer. Raman spectra were recorded using a 514 nm laser excitation on a Renishaw Raman spectrophotometer equipped with a LEICA microscope. XP spectra were measured on a SPECS spectrometer using a monochromatic X-Ray source (Al and Mg) operating at 200 W.

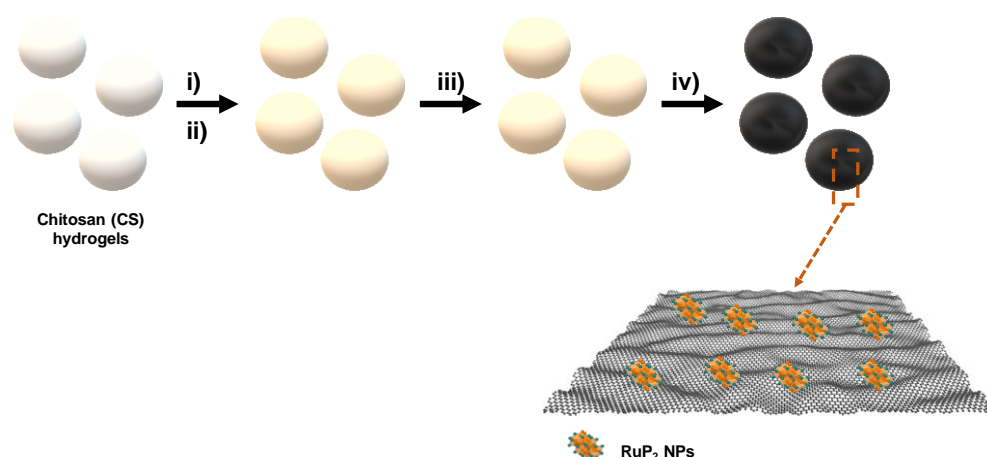
## 2.3. Electrochemical Measurements

Electrochemical measurements were performed in a conventional three-electrode electrochemical cell using an Ag/AgCl (3 M NaCl) reference electrode and a Pt wire auxiliary electrode. The working electrode was a catalyst-modified glassy carbon electrode (BAS, MF 2012, geometrical area 0.071 cm<sup>2</sup>, GCE). Voltammetric and EIS experiments were carried out with a CH 660I potentiostatic device (Cambria Scientific, Llwynhendy, Llanelli, Wales, UK). EIS measurements were carried out by superimposing different bias potentials to a sinusoidal excitation of 5 mV peak-to-peak amplitude in the 0.1 to 10<sup>5</sup> Hz frequency range. Air-saturated 0.5 M H<sub>2</sub>SO<sub>4</sub> and 1.0 M KOH aqueous solutions were used as electrolytes. The modification of the GCEs was initiated by polishing mechanically the bare GCE with 0.5 μm diamond down to 0.05 μm alumina slurry to obtain a mirror-like surface and then washed with Milli-Q water, ethanol and acetone and allowed to dry. Then, 10 μL of a suspension of the RuP<sub>2</sub>@N-P-C catalyst (5 mg·mL<sup>-1</sup>) in acetone plus nafion was dropped on the GCE and it was allowed to dry at air.

## 3. Results and Discussion

### Synthesis and Characterization of RuP<sub>2</sub>@N-P-C

RuP<sub>2</sub> nanoparticles embedded on graphitic porous N-P dual doped graphene were synthesized following a straightforward procedure. Briefly, an acidic chitosan (CS) solution was dropped into a concentrated NaOH solution to form CS microspheres of millimetric size. CS beads were then washed with water to neutralize the pH and the resulting hydrogels were impregnated with a RuCl<sub>3</sub> solution. CS hydrogels were immersed in RuCl<sub>3</sub> for 24 h, instead of dissolving CS in the metallic solution as an instantaneous gelation occurs when acetic acid is added to the CS suspension with Ru<sup>3+</sup>, thus, hindering the formation of microspheres in the subsequent steps because of the solution viscosity. Subsequently, the RuCl<sub>3</sub>/CS hydrogels were converted into alcogels by exchanging water with ethanol gradually at increasing ethanol/water ratios (from 10% to 100% ethanol). The as-obtained alcogels were then immersed for 24 h in a P<sub>2</sub>O<sub>5</sub> solution dissolved in ethanol. Superior adsorption efficiency of phosphate ions into CS matrix is a result of electrostatic interactions of protonated groups of CS and phosphate anions [31]. Drying under supercritical CO<sub>2</sub> conditions is in general preferred as it preserves the porosity of the beads preventing their shrinkage and collapse of their structure, thus affording light-weight and high surface area aerogels [26,41]. Scheme 1 illustrates the preparation process of the material.



**Scheme 1.** Schematic illustration of the synthesis of  $\text{RuP}_2@\text{NPC}$ , (i) impregnation of CS hydrogels with  $\text{RuCl}_3$  solution; (ii) impregnation of Ru containing CS beads with  $\text{P}_2\text{O}_5$ ; (iii) supercritical drying of CS-Ru-Phosphate beads and (iv) pyrolysis at  $900\text{ }^\circ\text{C}$  under inert atmosphere.

We first proceeded to prepare N,P-dual doped graphitic carbon beads without the addition of metals to see the effect of P doping on the surface area. Upon pyrolysis, highly porous graphitic 3D N,P-dual doped carbons are obtained. Figure S1 shows the structure of the beads obtained upon pyrolysis of CS beads containing phosphate ions. As it can be seen, N,P-dual doped graphitic carbon (N-P-C) contains domains of large porosity similar to KOH-treated carbons obtained from pyrolysis of CS [42,43]. Adding P to CS hydrogels was found to help increase the specific surface area due to the formation of  $\text{P}_2\text{O}_5$  that facilitates the gasification of carbon and distorts the graphitic structure [44]. We found that upon pyrolysis of phosphate-containing CS microspheres, the surface area increases from  $241\text{ m}^2\cdot\text{g}^{-1}$  for undoped CS beads to  $817\text{ m}^2\cdot\text{g}^{-1}$ . The increase observed upon pyrolysis of the beads verifies the role of  $\text{P}_2\text{O}_5$  as both a porogen agent and a dopant. Figure S2 shows the isotherm of  $\text{N}_2$  adsorption-desorption of N-P-C. Figure S3 shows the scanning transmission electron microscopy (STEM) images in bright field mode of N-P-C. The presence of holes in the layered material reveals the presence of a hierarchical porosity. To confirm the presence of the P element in the structure of N-P-C,  $^{31}\text{P}$  solid-state nuclear magnetic resonance (ss  $^{31}\text{P}$  NMR) spectroscopy was used. As it can be seen in Figure S4, the presence of a broad peak centered around  $-4.3\text{ ppm}$  reveals the presence of various polyphosphate species [32,45].

The addition of Ru results in a decrease of the surface area ( $765\text{ m}^2\cdot\text{g}^{-1}$ ), however the P amount contained in the material increases. Incorporation of multivalent cations into CS matrix generally leads to enhanced adsorption of phosphate ions explaining the increase in P content in  $\text{RuP}_2@\text{N-P-C}$  [31]. Table 1 summarizes the chemical composition of  $\text{RuP}_2@\text{N-P-C}$  and N-P-C as determined by elemental analysis and inductively coupled plasma-optical emission spectroscopy (ICP-OES).

**Table 1.** Chemical composition and surface area of N-P-C and  $\text{RuP}_2@\text{N-P-C}$ .

Sample	C (%)	N (%)	P (%)	Ru (%)	H (%)	Surface Area ( $\text{m}^2/\text{g}$ )
N-P-C	59.6	1.9	3.1	-	0.5	817
$\text{RuP}_2@\text{N-P-C}$	53.1	2	8.9	6.7	0.78	765

High-resolution field-emission scanning electron microscopy (HRFESEM) was used to examine the morphology of the as-obtained porous materials. As shown in Figure 1,  $\text{RuP}_2@\text{N-P-C}$  beads are shaped similarly to a Bristlecone pine. At high magnifications, a fibrillated morphology is revealed (Figure 1c). Associated energy-dispersive X-ray spec-



troscopy (EDX) images (Figure 1d and Figure S5) reveal that Ru, P and C elements are evenly distributed on the surface.

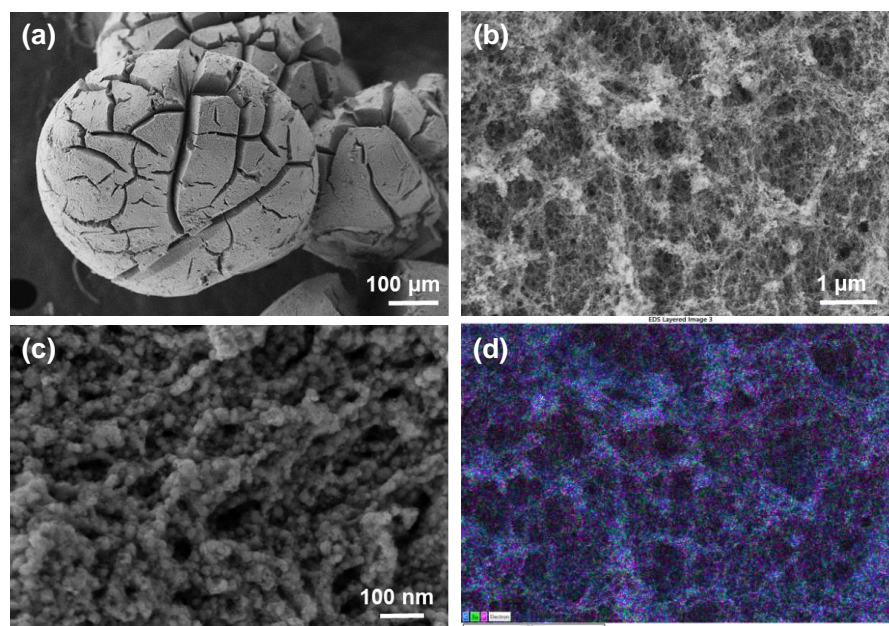


**Figure 1.** FESEM images (a–c) of RuP<sub>2</sub>@N-P-C at different magnifications and EDS layered image (d) showing the even distribution of C, Ru and P elements.

X-Ray diffraction was used to characterize the crystal structure of RuP<sub>2</sub>@N-P-C. As displayed in the XRD pattern of RuP<sub>2</sub>@NPC (Figure S6), the peaks depicted at 23°, 30.4°, 35°, 36.1°, 38.5°, 39.2°, 46.1°, 47.1°, 47.5°, 49.9°, 50.2°, 54.9°, 56.2°, 56.9°, 59.9°, 65.1°, 68.6°, 72.1°, 73.6°, 74.5° and 76.2° correspond to the (110), (020), (012), (101), (021), (111), (022), (112), (121), (013), (211), (031), (103), (122), (113), (200), (123), (202), (024), (114) and (041) planes of the orthorhombic RuP<sub>2</sub> phase, respectively [46,47].

Raman spectroscopy was used to assess the graphitization of the carbon obtained upon pyrolysis. Typical peaks observed around 2700, 1595 and 1354 cm<sup>-1</sup> in the Raman spectrum of RuP<sub>2</sub>@N-P-C (Figure S7) correspond to the 2D, G and D bands, respectively. The I<sub>D</sub>/I<sub>G</sub> ratio of 0.85 found for RuP<sub>2</sub>@N-P-C indicates the formation of a graphitized carbon instead of amorphous carbon [48,49].

X-Ray Photoelectron Spectroscopy was conducted to assess the surface chemical state as well as the surface elemental composition of RuP<sub>2</sub>@NPG. XPS analysis of RuP<sub>2</sub>@NPG reveals the presence of C, Ru, N, O and P. Figure 2 shows the high resolution XPS of the different elements present in RuP<sub>2</sub>@NPG. In the C1s spectrum, the peak centered at 284.5 eV corresponds to C=C, while the ones at 285.6, 286.5 and 289.1 eV correspond to C-N/C-P, C-O and O-C=O, respectively [50,51]. Ru3d<sub>5/2</sub> and Ru3d<sub>3/2</sub> occur at shifted binding energies than the ones expected at 280.2 eV and 284.4 eV. The experimental N1s peak can be deconvoluted into four components at 398.2, 400.1, 401.4 and 403.7 eV which are attributed to pyridinic N, pyrrolic N, graphitic N and oxidized N, respectively [51–53]. The components of the P2p spectrum at 130.1, 133 and 134.2 eV correspond to P-Ru, P-C and P-O, respectively [51,54]. The latter peak might be due to the presence of residual phosphates or from oxidized P-O species resulting from incomplete P reduction or formed during air exposure [52]. In the Ru3p spectrum, the peaks centered at 462.6 and 485.1 eV correspond to Ru3p<sub>3/2</sub> and Ru3p<sub>1/2</sub>, respectively. The peaks observed at 463.9 and 487.8 eV correspond to oxidized RuP<sub>2</sub> species due to unavoidable air exposure [53,54]. Regarding oxygen atoms, the experimental O1s peak can be deconvoluted into two components at 531 eV and 532.5 eV which are attributed to P-O and C-O bonds, respectively [45,55].

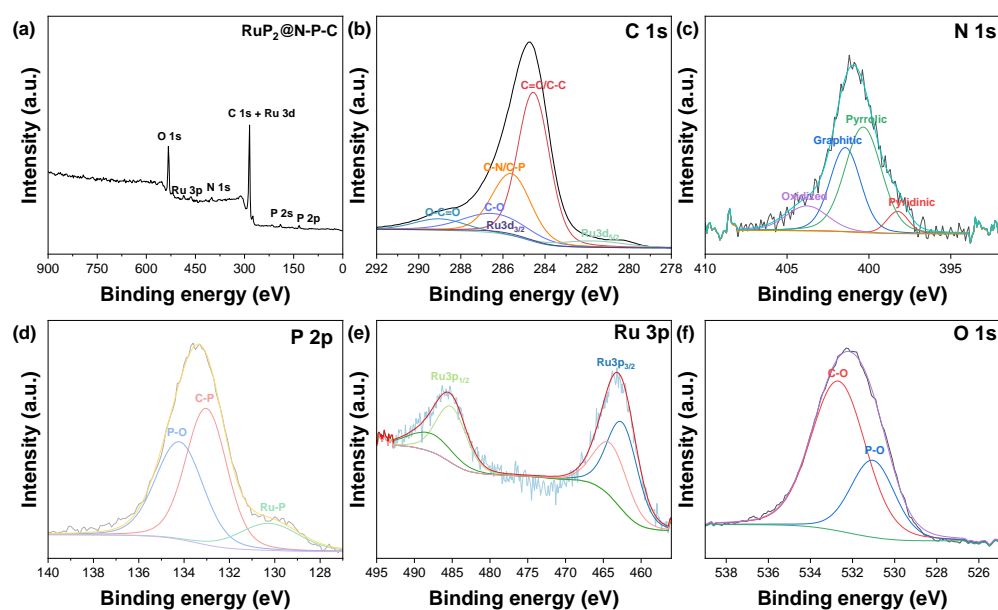


**Figure 2.** (a) XPS survey spectrum of RuP<sub>2</sub>@N-P-C. High-resolution XPS spectra of (b) C 1s, (c) N 1s, (d) P 2p and (e) Ru 3p and (f) O 1s.

High-resolution transmission electron microscopy (HRTEM) images reveal the layered nature of RuP<sub>2</sub>@N-P-C as well as the presence of nanoparticles of different sizes. (Figure 3a). HRTEM was used to further confirm the nature of ruthenium phosphide formed. Figure 3c evidences the presence of lattice fringes with a spacing of 0.258 nm corresponding to the (011) plane of orthorhombic RuP<sub>2</sub> [47]. Figure S8 shows the EDX spectrum of one of the nanoparticles analyzed. It was found that the elements composing the nanoparticle are Ru and P. Dark-field STEM (DF-STEM) images (Figure S9) reveal that RuP<sub>2</sub> nanoparticles of different sizes are evenly distributed on the N-P-C support. The average size of the nanoparticles determined by measuring a statistically relevant number of nanoparticles from HRFESEM and DF-STEM images is 8.7 nm ± 4.7 nm.

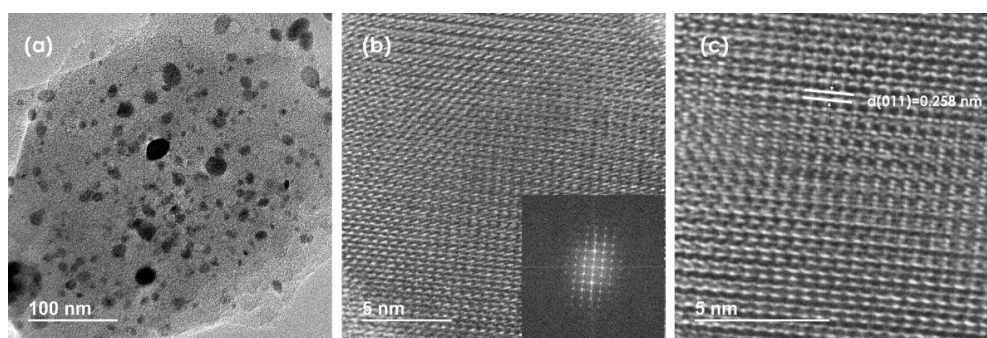


**Figure 3.** (a–c) HRTEM images of RuP<sub>2</sub>@N-P-C at different magnifications. The inset in the image (b) corresponds to the FFT spectrum of the electron diffraction from one RuP<sub>2</sub> nanoparticle supported on N-P-C.

#### 4. Electrochemistry

Figure 4 shows the negative-going linear potential scan voltammograms (LSVs) recorded at 5 mV·s<sup>-1</sup> for GCEs modified with RuP<sub>2</sub>@N-P-C (black) and Pt/C (red) in contact with 0.50 M H<sub>2</sub>SO<sub>4</sub> solution under stirring. One can see that the catalytic effect of HER exerted by RuP<sub>2</sub>@N-P-C, although comparable to that of 20% Pt/C, does not improve the onset potential. The Tafel analysis of the rising portion of the voltammetric wave, however, yields satisfactory values of the onset potential (−225 ± 5 vs. RHE), Tafel slope

( $27.1 \pm 0.6 \text{ mV.decade}^{-1}$ ), the exchange current ( $(1.0 \pm 0.3) \times 10^{-2} \text{ mA.cm}^{-2}$ ), and the overpotential at a current density of  $10 \text{ mA cm}^{-2}$  ( $-300 \pm 10 \text{ mV vs. RHE}$ ), when compared with other catalysts (see Table S1) in recent literature [34,35]. In contrast, in contact with 1.0 M KOH the performance of the RuP<sub>2</sub>@N-P-C- catalyst is clearly lower with that of Pt/C, as can be seen in Figure S10.

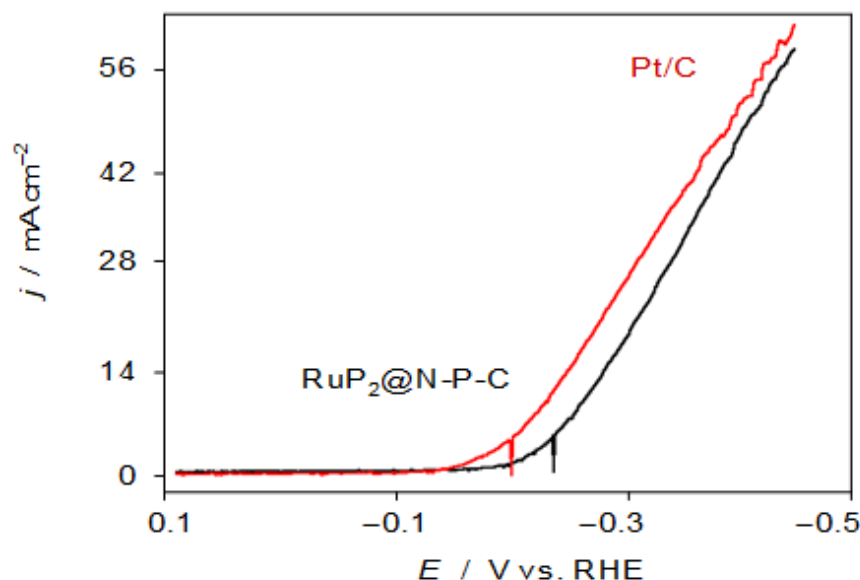
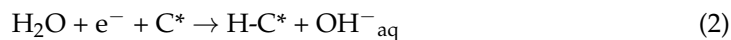


**Figure 4.** Negative-going LSVs of RuP<sub>2</sub>@N-P-C- (black) and Pt/C-modified (red) glassy carbon electrodes under stirring conditions (650 rpm) in contact with 0.50 M H<sub>2</sub>SO<sub>4</sub>. Potential scan rate 5 mV.s<sup>-1</sup>.

The difference in the electrocatalytic performance of RuP<sub>2</sub>@N-P-C in acidic and alkaline media can be rationalized on considering that the initial step (Volmer step) of HER in acidic media,

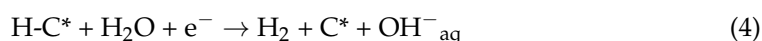
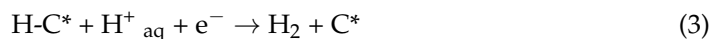


involves the adsorption of the generated H atom onto the surface of the catalyst active site (denoted by C\* in Equation (1)) [35]. In alkaline media, the concentration of hydrogen ions is drastically diminished and the Volmer step are likely to include a water-dissociation step [36,37],



Accordingly, in alkaline electrolytes, the cleavage of water O–H bond and the transport of OH<sup>-</sup> from the catalyst surface to the electrolyte would be part of the limiting step in the overall HER process [38].

Similar considerations can be applied to the subsequent step in the Volmer-Heyrovsky pathway which can be represented as,



in acidic (Equation (3)) and alkaline (Equation (4)) media, respectively. In the Volmer-Tafel pathway, however, the second step



should be minimally influenced by pH changes.

In this context, the importance of interfacial interactions has been emphasized [38] and the impact of alkali ions in HER at Pt and PtNi surfaces has been reported [39,40].

Accordingly, we explored the influence of  $\text{Li}^+$  ions on the catalytic activity of  $\text{RuP}_2@\text{N-P-C}$ . This effect can be clearly seen under quiescent conditions, as is illustrated in Figure S11. Here, the negative-going LSVs of  $\text{RuP}_2@\text{N-P-C}$ -modified GCE in contact with 0.50 M  $\text{H}_2\text{SO}_4$  and 0.50 M  $\text{H}_2\text{SO}_4 + 0.15$  M  $\text{LiClO}_4$  solutions are depicted. Although the voltammograms show irregular features due to the formation of  $\text{H}_2$  bubbles at relatively high overpotentials, one can see that the currents are markedly enhanced in the presence of  $\text{Li}^+$  ions in the electrolyte. Figure 5 shows the Tafel plots for 0.50 M  $\text{H}_2\text{SO}_4 + 0.15$  M  $\text{LiClO}_4$  and 0.50 M  $\text{H}_2\text{SO}_4 + 0.03$  M  $\text{LiClO}_4$  solutions, in both cases with satisfactory linearity in the  $\ln(j)$  vs.  $E$  plots.

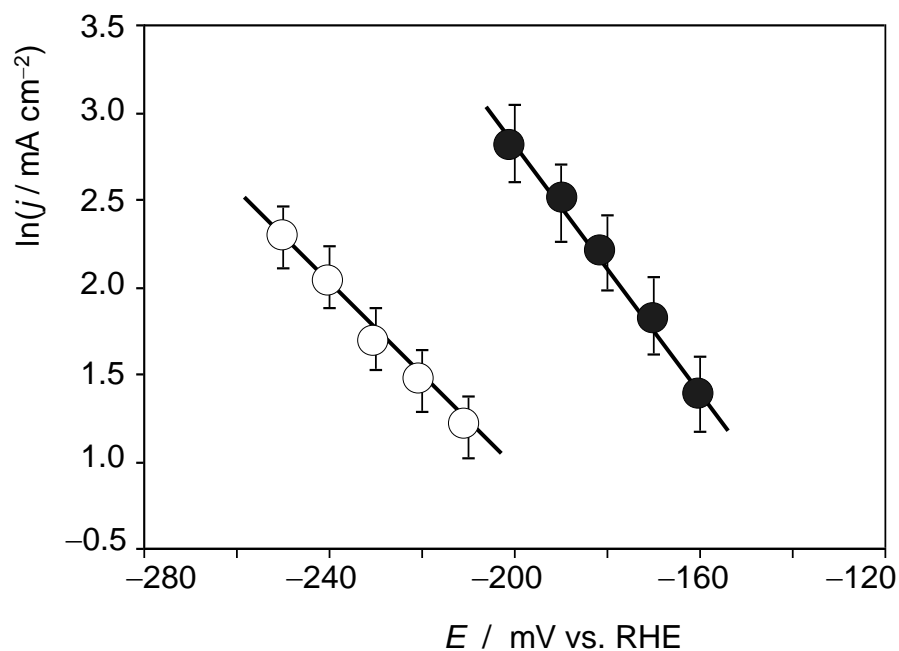


**Figure 5.** Tafel plots from the foot of the voltammetric curves recorded at  $\text{RuP}_2@\text{N-P-C}$ -modified GCEs immersed into 0.50 M  $\text{H}_2\text{SO}_4 + 0.15$  M  $\text{LiClO}_4$  (solid circles) and 0.50 M  $\text{H}_2\text{SO}_4 + 0.03$  M  $\text{LiClO}_4$  solutions (circles). Potential scan rate  $2 \text{ mV}\cdot\text{s}^{-1}$ . Averaged values from three replicate measurements.

Experimental data at different concentrations of  $\text{Li}^+$  reveal that the Tafel slope and the exchange current density increase with the concentration of alkali metal cation, whereas the onset potential remains essentially unchanged. Pertinent data can be seen in Table S1. Experiments at relatively large potential scan rates produced sigmoidal curves interrupted by the sharp transients associated to the formation of  $\text{H}_2$  bubbles over the electrode surface. This can be seen in Figure S12 where the CV of  $\text{RuP}_2@\text{N-P-C}$ -modified glassy carbon electrode recorded under quiescent conditions in contact with 0.50 M  $\text{H}_2\text{SO}_4 + 0.27$  M  $\text{LiClO}_4$  solution is presented. Qualitatively, the recorded CV response agrees with that theoretically described for electrocatalytic processes involving species in solution phase for large values of the rate constant  $k$  [56]:

$$i = \frac{nFAcD^{1/2} k^{1/2}}{1 + \exp\left[\frac{nE}{RT} (E - E_{1/2})\right]} \quad (6)$$

In this equation,  $c$  denotes the concentration of the electroactive species,  $D$  its diffusion coefficient and  $E_{1/2}$  the half-wave potential. At sufficiently high cathodic potentials, the above equation can be simplified to [56,57]:

$$i_{\text{lim}} = nFAcD^{1/2} k^{1/2} \quad (7)$$



i.e., the current tends to a limiting value ( $i_{lim}$ ) regardless the potential scan rate. Figure S13 illustrates the variation in the limiting current and the half-wave potential with the concentration of  $Li^+$  in 0.5 M  $H_2SO_4$  solutions.

Although the situation studied here involves a solid catalyst (i.e., differs from the electrocatalysis by species in solution), the above consideration can in principle be taken as a reasonable initial approximation. For our purposes, there are different aspects to emphasize:

(a) The HER process at  $RuP_2@N-P-C$ , a porous material, will involve some restricted diffusion of hydrogen ions in solution through the external region of the solid in order to be adsorbed onto the different active sites. This is supported by abundant literature describing the differences observed between continuous and discrete monolayers and multilayers of catalysts such as  $MoS_2$  [58].

(b) The diffusion of different ionic species through the layers of porous catalysts can be taken as analogous to that occurring in redox polymers [59–62] in which co-diffusion effects have to be considered [63–66]. As a result, different diffusive behaviors can operate.

(c) Co-diffusion effects can be rationalized pm considering that, in solution phase,  $H^+$  and  $Li^+$  are (mainly) in the form of  $H_3O^+$  and  $Li(H_2O)_n^+$  ions. Then, their penetration into the pores of the solid involves more or less extensive de-hydration. This process, and the subsequent ionic diffusion through the pores of the solid, could be particularly favorable for  $Li^+$ . Accordingly, although  $H^+$  diffusion is faster  $Li^+$  diffusion in the electrolyte, the transport of  $H^+$  through the porous material could be facilitated by the presumably faster diffusion of  $Li^+$  in the solid.

In this scenario, two extreme diffusive behaviors can be considered for the diffusion through two phases, electrolyte and porous catalyst: full coupling and absence of coupling between phases. The first situation operates at low electrolyte concentrations and the system experiences a Cottrell-type behavior with an effective diffusion coefficient,  $D_{eff}$ , given by:

$$D_{eff} = \frac{D_{solid} c_{solid} + D_{electrolyte} c_{electrolyte}}{c_{solid} + c_{electrolyte}} \quad (8)$$

where  $D_{solid}$ ,  $D_{electrolyte}$ , represent the diffusion coefficients of the diffusing species through the solid and the electrolyte and  $c_{solid}$ ,  $c_{electrolyte}$ , the respective concentrations. At high electrolyte concentrations and short times (typically shorter than 10–20 ms [59,60]), the flux of the diffusing species will be the sum of the independent diffusive contributions in each phase. Then, the system will display a Cottrell-type behavior characterized by the product between an effective concentration,  $c_{eff}$ , and the effective diffusion coefficient,  $D_{eff}$ , given by the expression:

$$c_{eff} D_{eff} = c_{solid} D_{solid}^{1/2} + c_{electrolyte} D_{electrolyte}^{1/2} \quad (9)$$

These situations have been studied for microparticulate films of dinuclear alkynyl-diphosphine Au(I) complexes [67] and Prussian blue [68].

The above expressions are analogue to those proposed for the co-diffusion of two electroactive species (A, B) in a unique phase [63–66]. Coupled diffusion is described by:

$$D_{eff} = \frac{D_A c_A + D_B c_B}{c_A + c_B} \quad (10)$$

Here,  $D_A$ ,  $D_B$ , represent the diffusion coefficients of the species A and B in the electrolyte and  $c_A$ ,  $c_B$ , their respective concentrations in this phase. When no coupled diffusion occurs,

$$c_{eff} D_{eff}^{1/2} = c_A D_A^{1/2} + c_B D_B^{1/2} \quad (11)$$

These situations have been experimentally tested for the particular case in which the A and B species are linked by an interconversion reaction [69].

A second effect on HER electrocatalysis associated to the presence of  $Li^+$  ions in the electrolyte can be considered: the co-adsorption. The effect of  $OH^-$ ,  $H_2O$  and cations co-adsorption on Pt surfaces has been studied with regard of HER [70–72]. Here, a variety of

factors have been balanced (formation of adducts, destabilization of  $\text{OH}_{\text{ads}}$ , partial charge retention, etc.), but further research is needed to achieve a complete view of this matter [38].

Qualitatively, these approaches can be applied to explain the accelerating effect of  $\text{Li}^+$  ions on HER at porous catalysts. Focusing our attention to the diffusive effects, and at the expense of the development of a detailed theoretical model, it is pertinent to note that if no coupling diffusion of  $\text{H}^+$  and  $\text{Li}^+$  ions occurs, no influence of  $\text{Li}^+$  on the HER process should take place. If coupled diffusion occurs, and if the diffusion of  $\text{Li}^+$  is faster than that of  $\text{H}^+$  through the porous film, the effect of  $\text{Li}^+$  would be the increase in the effective (co)diffusion of the system. Assuming that co-diffusion is operative, Equations (6) and (7) can be approximated by:

$$i = \frac{nFA (D_{\text{H}^+}c_{\text{H}^+} + D_{\text{Li}^+}c_{\text{Li}^+})^{1/2} k^{1/2}}{1 + \exp\left(\frac{nF}{RT} (E - E_{1/2})\right)} \quad (12)$$

$$i_{\text{lim}} = nFA (D_{\text{H}^+}c_{\text{H}^+} + D_{\text{Li}^+}c_{\text{Li}^+})^{1/2} k^{1/2} \quad (13)$$

where  $D_{\text{H}^+}$ ,  $D_{\text{Li}^+}$  are the diffusion coefficients of  $\text{H}^+$  and  $\text{Li}^+$  and  $c_{\text{H}^+}$ ,  $c_{\text{Li}^+}$  their respective concentrations in the electrolyte. Then, in experiments performed varying the concentration of  $\text{Li}^+$  at a constant concentration of hydrogen ions such as in Figure S13, taking  $i_{\text{lim}}^{\circ} = nFA D_{\text{H}^+}^{1/2} c_{\text{H}^+}^{1/2}$ , we obtain,

$$f(i_{\text{lim}}) = \frac{i_{\text{lim}} - i_{\text{lim}}^{\circ}}{i_{\text{lim}}^{\circ}} = \frac{(D_{\text{H}^+}c_{\text{H}^+} + D_{\text{Li}^+}c_{\text{Li}^+})^{1/2}}{(D_{\text{H}^+}c_{\text{H}^+})^{1/2}} \quad (14)$$

At large  $\text{Li}^+$  concentrations, Equation (14) tends to a linear variation in  $f(i_{\text{lim}})$  on the square root of the concentration of  $\text{Li}^+$  in the electrolyte. Figure 6 shows the variation in the  $f(i_{\text{lim}})$  ratio with the square root of the  $\text{Li}^+$  concentration resulting from voltammetric data such as depicted in Figure S12. One can see that the values at high  $\text{Li}^+$  concentrations can reasonably be fitted to a straight line. The slope of the linear plot ( $2.30 \pm 0.05$ ) permits to evaluate a  $(D_{\text{Li}^+}/D_{\text{H}^+})^{1/2}$  ratio of 4.6. This result implies that the diffusion is faster for  $\text{Li}^+$  than for  $\text{H}^+$ , an effect that can be understood assuming that the rate-determining step of the diffusional process is that occurring through the porous phosphide material. In short, this means that the porous material can accommodate more efficiently  $\text{Li}^+$  ions than adsorb hydrogen ions. At this stage, our results suggest that, despite the approximate character of the previous theoretical considerations, at least a part of the contribution of  $\text{Li}^+$  ions to promote HER at  $\text{RuP}_2@\text{N-P-C}$ -modified GCEs can be attributed to co-diffusion effects. A more detailed understanding of  $\text{Li}^+$  effect obviously requires further research to elucidate influence of adsorption and ion trapping processes.

EIS data were consistent with the foregoing set of considerations. When bias potentials separated from the proton discharge are applied, light differences were obtained  $\text{RuP}_2@\text{N-P-C}$ -modified GCEs immersed into 0.50 M  $\text{H}_2\text{SO}_4$  and 0.50 M  $\text{H}_2\text{SO}_4 + 0.14$  M  $\text{LiClO}_4$  solutions (Figure 7 and Supplementary Information, Figure S14). However, when the bias potential approaches those where the HER starts, the presence of  $\text{Li}^+$  ions in the electrolyte determines a decrease in the total impedance values at low frequencies. The Nyquist plots show two overlapping capacitive loops which can be fitted to the equivalent circuit shown in Figure S15. Remarkably, the negative increase in the bias potential does not alter significantly the high-frequency loop but determines important changes in the low-frequency region where the capacitive effects tend to vanish on increasing the hydrogen evolution. The charge transfer resistance values significantly decrease, and this decrease is larger as the  $\text{Li}^+$  concentration is, as can be seen in Figure S16 of supplementary Information for different bias potentials.

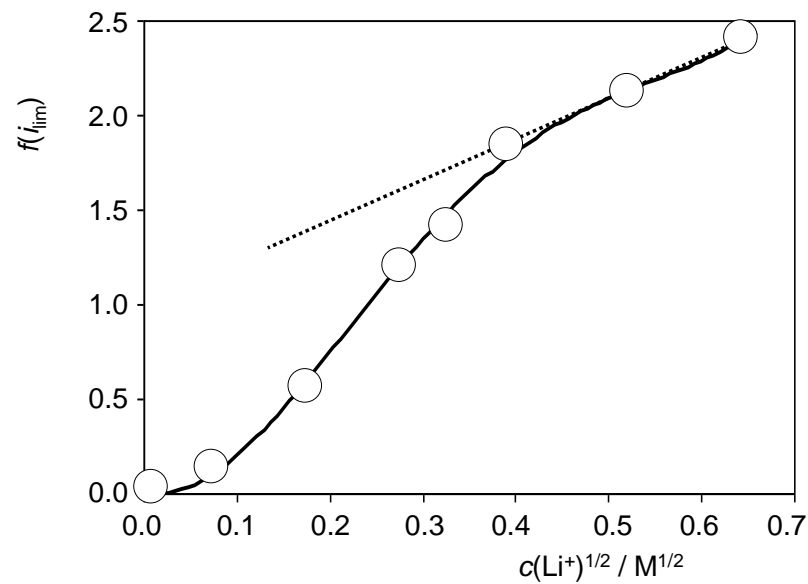


**Figure 6.** Variation in the  $f(i_{lim})$  ratio with the square root of the  $\text{Li}^+$  concentration in CVs at  $\text{RuP}_2@\text{N-P-C}$ -modified GCEs recorded under quiescent conditions in contact with  $0.50 \text{ M H}_2\text{SO}_4 + \text{LiClO}_4$  solutions in conditions such as those in Figure S12. The continuous line corresponds to the polynomial fit of the entire set of data while the dotted line defines the straight line fitting for the values at high concentrations of  $\text{Li}^+$ .

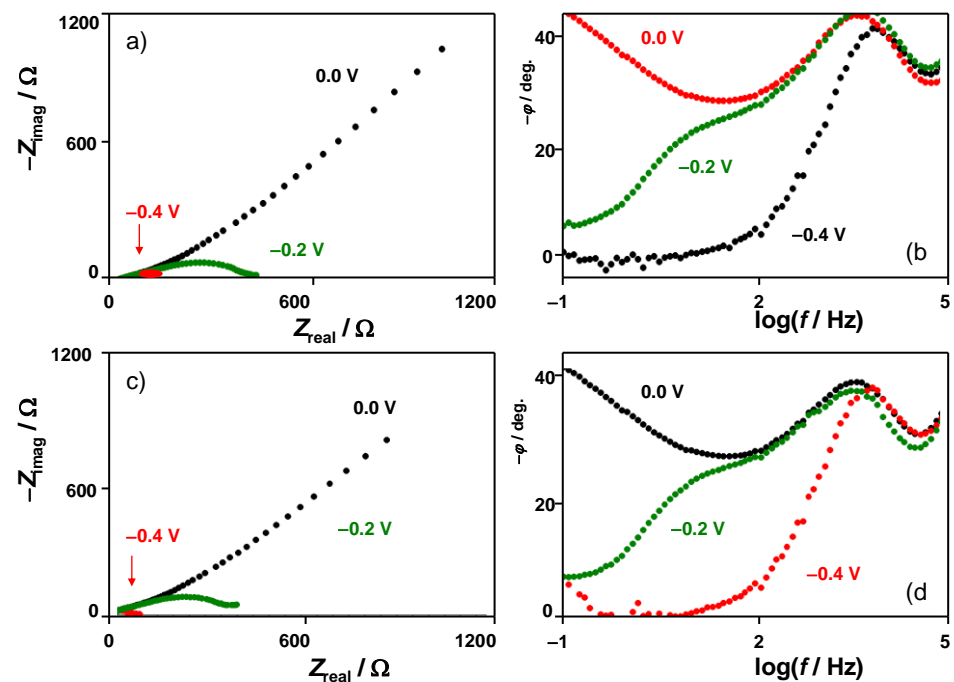


**Figure 7.** Impedance spectra of  $\text{RuP}_2@\text{N-P-C}$ -modified GCEs in contact with (a,b)  $0.50 \text{ M H}_2\text{SO}_4$  and (c,d)  $0.50 \text{ M H}_2\text{SO}_4 + 0.14 \text{ M LiClO}_4$  solutions at different bias potentials. (a,c) Nyquist plots of  $Z_{real}$  vs.  $-Z_{imag}$ ; (b,d) Bode plots of  $-\phi$  vs.  $\log f$ .

## 5. Conclusions

In this contribution, simultaneous P-doping and growth of crystalline ruthenium diphosphide was achieved through a straightforward approach consisting on the pyrolysis of  $\text{Ru}^{3+}$ -CS beads on which phosphate anions were previously co-adsorbed. Upon pyroly-

sis, highly porous N,P-dual-doped defective graphitic carbon on which crystalline RuP<sub>2</sub> nanoparticles are embedded was obtained. RuP<sub>2</sub>@N-P-C films deposited onto GCEs exert an electrocatalytic effect on HER in acidic media. This effect is significantly increased upon addition of Li<sup>+</sup> ions to the electrolyte. Voltammetric experiments at variable concentrations of this alkali cation suggest that co-diffusion effects, Li<sup>+</sup> diffusing faster than hydrogen ions through the porous catalyst can be responsible, at least partially, for this effect. The sustainable procedure proposed could be applied to prepare other non-precious metal phosphides supported on dual-doped highly porous graphitic carbons. Future studies should rely on the use of in situ/operando techniques [73] to further elucidate the dynamic changes occurring in the electrocatalysts during HER.

**Supplementary Materials:** The following supporting information can be downloaded at: <https://www.mdpi.com/article/10.3390/nano12203597/s1>, Figure S1. FESEM images of N,P-dual doped porous graphitic carbon (N-P-C). Figure S2. N<sub>2</sub> adsorption-desorption isotherm of N-P-C. Figure S3. Bright Field STEM images of N-P-C. Figure S4. <sup>31</sup>P SS NMR spectrum of N-P-C. Figure S5. FESEM image and associated EDX mapping of RuP<sub>2</sub>@N-P-C. Figure S6. XRD pattern of RuP<sub>2</sub>@N-P-C. Figure S7. Raman spectrum of RuP<sub>2</sub>@N-P-C. Figure S8. EDX spectrum of RuP<sub>2</sub>@N-P-C. Figure S9. Dark-field STEM images of RuP<sub>2</sub>@N-P-C. Figure S10. Negative-going LSVs of RuP<sub>2</sub>@N-P-C (red) and Pt/C-modified (black) glassy carbon electrodes under stirring conditions (650 rpm) in contact with 1.0 M KOH. Potential scan rate 5 mV.s<sup>-1</sup>. Figure S11. Negative-going LSVs of RuP<sub>2</sub>@N-P-C modified GCE in contact with 0.50 M H<sub>2</sub>SO<sub>4</sub> (red) and 0.50 M H<sub>2</sub>SO<sub>4</sub> + 0.15 M LiClO<sub>4</sub> under quiescent conditions. Potential scan rate 2 mV.s<sup>-1</sup>. Figure S12. CV of RuP<sub>2</sub>@N-P-C-modified glassy carbon electrode recorded under quiescent conditions in contact with 0.50 M H<sub>2</sub>SO<sub>4</sub> + 0.27 M LiClO<sub>4</sub> solution. Potential scan initiated at 0.30 V vs. RHE in the negative direction; potential scan rate 50 mV.s<sup>-1</sup>. The arrows mark the ascending (initial cathodic scan) and descending (subsequent positive-going scan) branches of the CV. Figure S13. Variation in: (a) the limiting current and (b) the half-wave potential with the concentration of Li<sup>+</sup> in CVs at RuP<sub>2</sub>@N-P-C-modified GCEs recorded under quiescent conditions in contact with 0.50 M H<sub>2</sub>SO<sub>4</sub> + LiClO<sub>4</sub> solutions. Potential scan initiated at 0.30 V vs. RHE in the negative direction; potential scan rate 50 mV.s<sup>-1</sup>. Figure S14. Nyquist plots of RuP<sub>2</sub>@N-P-C-modified GCEs recorded under quiescent conditions in contact with 0.50 M H<sub>2</sub>SO<sub>4</sub> and 0.50 M H<sub>2</sub>SO<sub>4</sub> + 0.14 M LiClO<sub>4</sub> solutions. Bias potential 0.40 V vs. RHE. The inset shows the magnified view of the high frequency region. Figure S15. Nyquist plots of RuP<sub>2</sub>@N-P-C-modified GCEs recorded under quiescent conditions in contact with a) 0.50 M H<sub>2</sub>SO<sub>4</sub> and b) 0.50 M H<sub>2</sub>SO<sub>4</sub> + 0.14 M LiClO<sub>4</sub> solutions. Bias potential 0.20 V vs. RHE. Experimental data points (black circles) are superimposed to the theoretical impedance spectra (continuous lines) based on the fit of experimental data to the equivalent circuit in c). This equivalent circuit contains the solution resistance (R<sub>s</sub>) in series with two parallel RC units, the first one contains the charge transfer resistance (R<sub>ct</sub>) and the double-layer capacitance (C<sub>dl</sub>); the second can be associated to the porous RuP<sub>2</sub>@N-P-C modifier. Its impedance is constituted by a porous resistance (R<sub>por</sub>) and a non-ideal capacitance element, represented by a constant phase element (Q<sub>por</sub>). Table S1. Comparison of the catalytic parameters of RuP<sub>2</sub>@N-P-C with other HER catalysts. Figure S16. Variation in the R<sub>por</sub> determined after fitting the experimental impedance spectra recorded at RuP<sub>2</sub>@N-P-C-modified GCEs in contact with 0.50 M H<sub>2</sub>SO<sub>4</sub> plus LiClO<sub>4</sub> solutions with the Li<sup>+</sup> concentration at different bias potentials.

**Author Contributions:** Conceptualization, A.A., A.D.-C. and H.G.; methodology, A.A. and A.D.-C.; software, A.A. and A.D.-C.; validation, A.D.-C. and H.G.; formal analysis, A.A. and A.D.-C.; investigation, A.A. and A.D.-C.; resources, A.D.-C. and H.G.; data curation, A.A. and A.D.-C.; writing—original draft preparation, A.A. and A.D.-C.; writing—review and editing, A.A., A.D.-C. and H.G.; supervision, A.D.-C. and H.G.; funding acquisition, A.D.-C. and H.G. All authors have read and agreed to the published version of the manuscript.

**Funding:** Financial support by the Spanish Ministry of Science and Innovation (PDI2022- 1260710B-C21 and Severo Ochoa) and the Generalitat Valenciana (Prometeo 2021-038) are gratefully acknowledged. A.A. thanks assistance from Erasmus+ for partial support of her stay at Valencia. The European Commission is acknowledged for partial funding through the ECO2Fuel project.

**Data Availability Statement:** Not applicable.

**Acknowledgments:** UEMF is acknowledged for financial support. A.A. thanks UEMF and UPV for an Erasmus+ 2019-1-ES01-KA107-062073 Scholarship.

**Conflicts of Interest:** The authors declare no conflict of interest. The funders had no role in the design of the study; in the collection, analyses, or interpretation of data; in the writing of the manuscript; or in the decision to publish the results.

## References

1. McGlade, C.; Ekins, P. The geographical distribution of fossil fuels unused when limiting global warming to 2 °C. *Nature* **2015**, *517*, 187–190. [[CrossRef](#)] [[PubMed](#)]
2. Welsby, D.; Price, J.; Pye, S.; Ekins, P. Unextractable fossil fuels in a 1.5 °C world. *Nature* **2021**, *597*, 230–234. [[CrossRef](#)] [[PubMed](#)]
3. Hosseini, S.E.; Wahid, M.A. Hydrogen production from renewable and sustainable energy resources: Promising green energy carrier for clean development. *Renew. Sustain. Energy Rev.* **2016**, *57*, 850–866. [[CrossRef](#)]
4. Turner, J.A. Sustainable Hydrogen Production. *Science* **2004**, *305*, 972–974. [[CrossRef](#)] [[PubMed](#)]
5. Boretti, A.; Banik, B.K. Advances in Hydrogen Production from Natural Gas Reforming. *Adv. Sustain. Syst.* **2021**, *2*, 2100097. [[CrossRef](#)]
6. LeValley, T.L.; Richard, A.R.; Fan, M. The progress in water gas shift and steam reforming hydrogen production technologies—A review. *Int. J. Hydrog. Energy* **2014**, *39*, 16983–17000. [[CrossRef](#)]
7. Wang, S.; Lu, A.; Zhong, C.-J. Hydrogen production from water electrolysis: Role of catalysts. *Nano Conver.* **2021**, *8*, 4. [[CrossRef](#)]
8. Tiwari, J.N.; Sultan, S.; Myung, C.W.; Yoon, T.; Li, N.; Ha, M.; Harzandi, A.M.; Park, H.J.; Kim, D.Y.; Chandrasekaran, S.S.; et al. Multicomponent electrocatalyst with ultralow Pt loading and high hydrogen evolution activity. *Nat. Energy* **2018**, *3*, 773–782. [[CrossRef](#)]
9. Zou, X.; Zhang, Y. Noble metal-free hydrogen evolution catalysts for water splitting. *Chem. Soc. Rev.* **2015**, *44*, 5148–5180. [[CrossRef](#)]
10. Mahmood, N.; Yao, Y.; Zhang, J.-W.; Pan, L.; Zhang, X.; Zou, J.-J. Electrocatalysts for Hydrogen Evolution in Alkaline Electrolytes: Mechanisms, Challenges, and Prospective Solutions. *Adv. Sci.* **2018**, *5*, 1700464. [[CrossRef](#)]
11. Mahmood, J.; Li, F.; Jung, S.-M.; Okyay, M.S.; Ahmad, I.; Kim, S.-J.; Park, N.; Jeong, H.Y.; Baek, J.-B. An efficient and pH-universal ruthenium-based catalyst for the hydrogen evolution reaction. *Nat. Nanotechnol.* **2017**, *12*, 441–446. [[CrossRef](#)]
12. Tiwari, J.N.; Harzandi, A.M.; Ha, M.; Sultan, S.; Myung, C.W.; Park, H.J.; Kim, D.Y.; Thangavel, P.; Singh, A.N.; Sharma, P.; et al. High-Performance Hydrogen Evolution by Ru Single Atoms and Nitrided-Ru Nanoparticles Implanted on N-Doped Graphitic Sheet. *Adv. Energy Mater.* **2019**, *9*, 1900931. [[CrossRef](#)]
13. Tiwari, J.N.; Dang, N.K.; Sultan, S.; Thangavel, P.; Jeong, H.Y.; Kim, K.S. Multi-heteroatom-doped carbon from waste-yeast biomass for sustained water splitting. *Nat. Sustain.* **2020**, *3*, 556–563. [[CrossRef](#)]
14. Bae, S.-Y.; Mahmood, J.; Jeon, I.-Y.; Baek, J.-B. Recent advances in ruthenium-based electrocatalysts for the hydrogen evolution reaction. *Nanoscale Horiz.* **2020**, *5*, 43–56. [[CrossRef](#)]
15. Yang, Y.; Wu, D.; Yu, Y.; Li, J.; Rao, P.; Jia, C.; Liu, Z.; Chen, Q.; Huang, W.; Luo, J.; et al. Bridge the activity and durability of Ruthenium for hydrogen evolution reaction with the RuOC link. *Chem. Eng. J.* **2022**, *433*, 134421. [[CrossRef](#)]
16. Shi, Y.; Zhang, B. Recent advances in transition metal phosphide nanomaterials: Synthesis and applications in hydrogen evolution reaction. *Chem. Soc. Rev.* **2016**, *45*, 1529–1541. [[CrossRef](#)]
17. Tiwari, J.N.; Dang, N.K.; Park, H.J.; Sultan, S.; Kim, M.G.; Haiyan, J.; Lee, Z.; Kim, K.S. Remarkably enhanced catalytic activity by the synergistic effect of palladium single atoms and palladium-cobalt phosphide nanoparticles. *Nano Energy* **2020**, *78*, 105166. [[CrossRef](#)]
18. Yu, Z.; Wei, X.-K.; Xu, J.; Li, Y.; Araujo, A.; Faria, J.L.; Dunin-Borkowski, R.E.; Liu, L. Multifunctional Noble Metal Phosphide Electrocatalysts for Organic Molecule Electro-Oxidation. *ACS Appl. Energy Mater.* **2021**, *4*, 1593–1600. [[CrossRef](#)]
19. Zhao, X.; Kong, X.; Liu, Z.; Li, Z.; Xie, Z.; Wu, Z.; He, F.; Chang, X.; Yang, P.; Zheng, J.; et al. The cutting-edge phosphorus-rich metal phosphides for energy storage and conversion. *Nano Today* **2021**, *40*, 101245. [[CrossRef](#)]
20. Chang, Q.; Ma, J.; Zhu, Y.; Li, Z.; Xu, D.; Duan, X.; Peng, W.; Li, Y.; Zhang, G.; Zhang, F.; et al. Controllable Synthesis of Ruthenium Phosphides (RuP and RuP<sub>2</sub>) for pH-Universal Hydrogen Evolution Reaction. *ACS Sustain. Chem. Eng.* **2018**, *6*, 6388–6394. [[CrossRef](#)]
21. Wang, J.; Kong, H.; Zhang, J.; Hao, Y.; Shao, Z.; Ciucci, F. Carbon-based electrocatalysts for sustainable energy applications. *Prog. Mater. Sci.* **2021**, *116*, 100717. [[CrossRef](#)]
22. Kweon, D.H.; Okyay, M.S.; Kim, S.-J.; Jeon, J.-P.; Noh, H.-J.; Park, N.; Mahmood, J.; Baek, J.-B. Ruthenium anchored on carbon nanotube electrocatalyst for hydrogen production with enhanced Faradaic efficiency. *Nat. Commun.* **2020**, *11*, 1278. [[CrossRef](#)]
23. Liu, T.; Wang, S.; Zhang, Q.; Chen, L.; Hu, W.; Li, C.M. Ultrasmall Ru<sub>2</sub>P nanoparticles on graphene: A highly efficient hydrogen evolution reaction electrocatalyst in both acidic and alkaline media. *Chem. Commun.* **2018**, *54*, 3343–3346. [[CrossRef](#)] [[PubMed](#)]
24. Teller, H.; Krichevski, O.; Gur, M.; Gedanken, A.; Schechter, A. Ruthenium Phosphide Synthesis and Electroactivity toward Oxygen Reduction in Acid Solutions. *ACS Catal.* **2015**, *5*, 4260–4267. [[CrossRef](#)]
25. El Kadib, A. Chitosan as a Sustainable Organocatalyst: A Concise Overview. *ChemSusChem* **2015**, *8*, 217–244. [[CrossRef](#)] [[PubMed](#)]



26. El Kadib, A. Green and Functional Aerogels by Macromolecular and Textural Engineering of Chitosan Microspheres. *Chem. Rec.* **2020**, *20*, 753–772. [[CrossRef](#)]
27. Primo, A.; Sánchez, E.; Delgado, J.M.; García, H. High-yield production of N-doped graphitic platelets by aqueous exfoliation of pyrolyzed chitosan. *Carbon* **2014**, *68*, 777–783. [[CrossRef](#)]
28. Anouar, A.; Ramírez Grau, R.; Katir, N.; Franconetti, A.; El Kadib, A.; Primo, A.; García, H. Nanometer-thick defective graphene films decorated with oriented ruthenium nanoparticles. Higher activity of 101 vs 002 plane for silane-alcohol coupling and hydrogen transfer reduction. *J. Catal.* **2022**, *407*, 342–352. [[CrossRef](#)]
29. Wang, J.; Kim, J.; Choi, S.; Wang, H.; Lim, J. A Review of Carbon-Supported Nonprecious Metals as Energy-Related Electrocatalysts. *Small Methods* **2020**, *4*, 2000621. [[CrossRef](#)]
30. Liu, X.; Zhang, L. Removal of phosphate anions using the modified chitosan beads: Adsorption kinetic, isotherm and mechanism studies. *Powder Technol.* **2015**, *277*, 112–119. [[CrossRef](#)]
31. Eltaweil, A.S.; Omer, A.M.; El-Aqapa, H.G.; Gaber, N.M.; Attia, N.F.; El-Subruiti, G.M.; Mohy-Eldin, M.S.; Abd El-Monaem, E.M. Chitosan based adsorbents for the removal of phosphate and nitrate: A critical review. *Carbohydr. Polym.* **2021**, *274*, 118671. [[CrossRef](#)] [[PubMed](#)]
32. Anouar, A.; Grirrane, A.; Álvarez, E.; Katir, N.; Primo, A.; Garcia, H.; El Kadib, A. Nanosized copper stabilized on ternary P, N, S-doped graphene from chitosan shellfish waste: Preparation and catalysis of single and double A3-type amine coupling. *Mater. Today Sustain.* **2022**, *18*, 100109. [[CrossRef](#)]
33. Chen, X.; Liu, Q.; Zhang, M.; Ju, H.; Zhu, J.; Qiao, Q.; Wang, M.; Yang, S. Noncovalent phosphorylation of graphene oxide with improved hole transport in high-efficiency polymer solar cells. *Nanoscale* **2018**, *10*, 14840–14846. [[CrossRef](#)]
34. Gao, M.-R.; Liang, J.-X.; Zheng, Y.-R.; Xu, Y.-F.; Jiang, J.; Gao, Q.; Li, J.; Yu, S.-H. An efficient molybdenum disulfide/cobalt diselenide hybrid catalyst for electrochemical hydrogen generation. *Nat. Commun.* **2015**, *6*, 5982. [[CrossRef](#)]
35. Ding, Q.; Song, B.; Xu, P.; Jin, S. Efficient Electrocatalytic and Photoelectrochemical Hydrogen Generation Using MoS<sub>2</sub> and Related Compounds. *Chem* **2016**, *1*, 699–726. [[CrossRef](#)]
36. Zheng, Y.; Jiao, Y.; Vasileff, A.; Qiao, S.-Z. The Hydrogen Evolution Reaction in Alkaline Solution: From Theory, Single Crystal Models, to Practical Electrocatalysts. *Angew. Chem. Int. Ed.* **2018**, *57*, 7568–7579. [[CrossRef](#)] [[PubMed](#)]
37. Subbaraman, R.; Tripkovic, D.; Strmcnik, D.; Chang, K.-C.; Uchimura, M.; Paulikas, A.P.; Stamenkovic, V.; Markovic, N.M. Enhancing Hydrogen Evolution Activity in Water Splitting by Tailoring Li+Ni(OH)<sub>2</sub>-Pt Interfaces. *Science* **2011**, *334*, 1256–1260. [[CrossRef](#)]
38. Dubouis, N.; Grimaud, A. The hydrogen evolution reaction: From material to interfacial descriptors. *Chem. Sci.* **2019**, *10*, 9165–9181. [[CrossRef](#)]
39. Liu, E.; Li, J.; Jiao, L.; Doan, H.T.T.; Liu, Z.; Zhao, Z.; Huang, Y.; Abraham, K.M.; Mukerjee, S.; Jia, Q. Unifying the Hydrogen Evolution and Oxidation Reactions Kinetics in Base by Identifying the Catalytic Roles of Hydroxyl-Water-Cation Adducts. *J. Am. Chem. Soc.* **2019**, *141*, 3232–3239. [[CrossRef](#)]
40. Weber, D.J.; Janssen, M.; Oezaslan, M. Effect of Monovalent Cations on the HOR/HER Activity for Pt in Alkaline Environment. *J. Electrochem. Soc.* **2019**, *166*, F66–F73. [[CrossRef](#)]
41. Anouar, A.; Katir, N.; El Kadib, A.; Primo, A.; García, H. Palladium Supported on Porous Chitosan–Graphene Oxide Aerogels as Highly Efficient Catalysts for Hydrogen Generation from Formate. *Molecules* **2019**, *24*, 3290. [[CrossRef](#)] [[PubMed](#)]
42. Primo, A.; Forneli, A.; Corma, A.; García, H. From Biomass Wastes to Highly Efficient CO<sub>2</sub> Adsorbents: Graphitisation of Chitosan and Alginate Biopolymers. *ChemSusChem* **2012**, *5*, 2207–2214. [[CrossRef](#)] [[PubMed](#)]
43. Zhu, Y.-P.; Liu, Y.; Liu, Y.-P.; Ren, T.-Z.; Chen, T.; Yuan, Z.-Y. Direct Synthesis of Phosphorus-Doped Mesoporous Carbon Materials for Efficient Electrocatalytic Oxygen Reduction. *ChemCatChem* **2015**, *7*, 2903–2909. [[CrossRef](#)]
44. Liu, G.; Liu, Z.; Li, J.; Zeng, M.; Li, Z.; He, L.; Li, F. Chitosan/phytic acid hydrogel as a platform for facile synthesis of heteroatom-doped porous carbon frameworks for electrocatalytic oxygen reduction. *Carbon* **2018**, *137*, 68–77. [[CrossRef](#)]
45. Anouar, A.; Katir, N.; Mamede, A.-S.; Aboulaich, A.; Draoui, K.; Royer, S.; El Kadib, A. Synthesis and multifaceted use of phosphorylated graphene oxide: Growth of titanium dioxide clusters, interplay with gold nanoparticles and exfoliated sheets in bioplastics. *Mater. Chem. Front.* **2019**, *3*, 242–250. [[CrossRef](#)]
46. Pu, Z.; Amiin, I.S.; Kou, Z.; Li, W.; Mu, S. RuP<sub>2</sub>-Based Catalysts with Platinum-like Activity and Higher Durability for the Hydrogen Evolution Reaction at All pH Values. *Angew. Chem. Int. Ed.* **2017**, *56*, 11559–11564. [[CrossRef](#)]
47. Guo, Z.; Li, J.; Qi, H.; Sun, X.; Li, H.; Tamirat, A.G.; Liu, J.; Wang, Y.; Wang, L. A Highly Reversible Long-Life Li–CO<sub>2</sub> Battery with a RuP<sub>2</sub>-Based Catalytic Cathode. *Small* **2019**, *15*, 1803246. [[CrossRef](#)]
48. He, J.; Anouar, A.; Primo, A.; García, H. Quality Improvement of Few-Layers Defective Graphene from Biomass and Application for H<sub>2</sub> Generation. *Nanomaterials* **2019**, *9*, 895. [[CrossRef](#)]
49. Wang, J.; Gao, Y.; You, T.L.; Ciucci, F. Bimetal-decorated nanocarbon as a superior electrocatalyst for overall water splitting. *J. Power Sources* **2018**, *401*, 312–321. [[CrossRef](#)]
50. Wu, H.; Geng, J.; Ge, H.; Guo, Z.; Wang, Y.; Zheng, G. Egg-Derived Mesoporous Carbon Microspheres as Bifunctional Oxygen Evolution and Oxygen Reduction Electrocatalysts. *Adv. Energy Mater.* **2016**, *6*, 1600794. [[CrossRef](#)]
51. Wang, J.; Ciucci, F. In-situ synthesis of bimetallic phosphide with carbon tubes as an active electrocatalyst for oxygen evolution reaction. *Appl. Catal. B* **2019**, *254*, 292–299. [[CrossRef](#)]

52. Pu, Z.; Zhao, J.; Amiin, I.S.; Li, W.; Wang, M.; He, D.; Mu, S. A universal synthesis strategy for P-rich noble metal diphosphide-based electrocatalysts for the hydrogen evolution reaction. *Energy Environ. Sci.* **2019**, *12*, 952–957. [[CrossRef](#)]
53. Zhou, F.; Sa, R.; Zhang, X.; Zhang, S.; Wen, Z.; Wang, R. Robust ruthenium diphosphide nanoparticles for pH-universal hydrogen evolution reaction with platinum-like activity. *Appl. Catal. B* **2020**, *274*, 119092. [[CrossRef](#)]
54. Luo, Q.; Xu, C.; Chen, Q.; Wu, J.; Wang, Y.; Zhang, Y.; Fan, G. Synthesis of ultrafine ruthenium phosphide nanoparticles and nitrogen/phosphorus dual-doped carbon hybrids as advanced electrocatalysts for all-pH hydrogen evolution reaction. *Int. J. Hydrog. Energy* **2019**, *44*, 25632–25641. [[CrossRef](#)]
55. Li, Y.; Li, S.; Wang, Y.; Wang, J.; Liu, H.; Liu, X.; Wang, L.; Liu, X.; Xue, W.; Ma, N. Electrochemical synthesis of phosphorus-doped graphene quantum dots for free radical scavenging. *Phys. Chem. Chem. Phys.* **2017**, *19*, 11631–11638. [[CrossRef](#)]
56. Nicholson, R.S.; Shain, I. Theory of Stationary Electrode Polarography—Single Scan and Cyclic Methods Applied to Reversible, Irreversible, and Kinetic Systems. *Anal. Chem.* **1964**, *36*, 706–723. [[CrossRef](#)]
57. Savéant, J.M.; Vianello, E. Recherches sur les courants catalytiques en polarographie—Oscillographique à balayage linéaire de tension. Etude Théorique. In *Advances in Polarography*; Longmuir, I.S., Ed.; Pergamon: Oxford, UK, 1960; pp. 367–374.
58. Li, G.; Zhang, D.; Qiao, Q.; Yu, Y.; Peterson, D.; Zafar, A.; Kumar, R.; Curtarolo, S.; Hunte, F.; Shannon, S.; et al. All The Catalytic Active Sites of MoS<sub>2</sub> for Hydrogen Evolution. *J. Am. Chem. Soc.* **2016**, *138*, 16632–16638. [[CrossRef](#)]
59. Andrieux, C.P.; Hapiot, P.; Savéant, J.M. Electron-transfer coupling of diffusional pathways: Theory for potential step chronoamperometry and chronocoulometry. *J. Electroanal. Chem. Interf. Electrochem.* **1984**, *172*, 49–65. [[CrossRef](#)]
60. Miller, C.J.; Majda, M. Microporous aluminum oxide films at electrodes part II. studies of electron transport in the Al<sub>2</sub>O<sub>3</sub> matrix derivatized by adsorption of poly(4-vinylpyridine). *J. Electroanal. Chem. Interf. Electrochem.* **1986**, *207*, 49–72. [[CrossRef](#)]
61. Miller, C.J.; Majda, M. Microporous aluminum oxide films at electrodes. Dynamics of ascorbic acid oxidation mediated by ferricyanide ions bound electrostatically in bilayer assemblies of octadecyltrichlorosilane and an octadecylviologen amphiphile. *Anal. Chem.* **1988**, *60*, 1168–1176. [[CrossRef](#)]
62. Guidelli, R.; Cozzi, D. Homogeneous chemical equilibria in polarography. II. Examples. *J. Phys. Chem.* **1967**, *71*, 3027–3034. [[CrossRef](#)]
63. De Jong, H.G.; Van Leeuwen, H.P.; Holub, K. Voltammetry of metal complex systems with different diffusion coefficients of the species involved: Part I. Analytical approaches to the limiting current for the general case including association/dissociation kinetics. *J. Electroanal. Chem. Interf. Electrochem.* **1987**, *234*, 1–16. [[CrossRef](#)]
64. Evans, D.H. Multicomponent diffusion with chemical reactions and its effect in voltammetry. *J. Electroanal. Chem. Interf. Electrochem.* **1989**, *258*, 451–456. [[CrossRef](#)]
65. Blauch, D.N.; Anson, F.C. Effects of interconversion and electron transfer on voltammetric responses for two-component systems with differing diffusion coefficients. *J. Electroanal. Chem. Interf. Electrochem.* **1991**, *309*, 313–318. [[CrossRef](#)]
66. Oldham, K.B. Steady-state microelectrode voltammetry as a route to homogeneous kinetics. *J. Electroanal. Chem. Interf. Electrochem.* **1991**, *313*, 3–16. [[CrossRef](#)]
67. Doménech-Carbó, A.; Koshevoy, I.O.; Montoya, N.; Pakkanen, T.A.; Doménech-Carbó, M.T. Solvent-Independent Electrode Potentials of Solids Undergoing Insertion Electrochemical Reactions: Part II. Experimental Data for Alkynyl-diphosphine Dinuclear Au(I) Complexes Undergoing Electron Exchange Coupled to Anion Exchange. *J. Phys. Chem. C* **2012**, *116*, 25984–25992. [[CrossRef](#)]
68. Doménech-Carbó, A.; Scholz, F.; Montoya, N. Solvent-Independent Electrode Potentials of Solids Undergoing Insertion Electrochemical Reactions: Part III. Experimental Data for Prussian Blue Undergoing Electron Exchange Coupled to Cation Exchange. *J. Phys. Chem. C* **2012**, *116*, 25993–25999. [[CrossRef](#)]
69. Doménech, A.; García-España, E.; Navarro, P.; Reviriego, F. Electrochemical determination of the stability of complexes formed by proton-ionizable ligands of 3,5-disubstituted 1H-pyrazole with phenethylamine. *Talanta* **2000**, *51*, 625–636. [[CrossRef](#)]
70. van der Niet, M.J.T.C.; Garcia-Araez, N.; Hernández, J.; Feliu, J.M.; Koper, M.T.M. Water dissociation on well-defined platinum surfaces: The electrochemical perspective. *Catal. Today* **2013**, *202*, 105–113. [[CrossRef](#)]
71. McCrum, I.T.; Janik, M.J. pH and Alkali Cation Effects on the Pt Cyclic Voltammogram Explained Using Density Functional Theory. *J. Phys. Chem. C* **2016**, *120*, 457–471. [[CrossRef](#)]
72. Chen, X.; McCrum, I.T.; Schwarz, K.A.; Janik, M.J.; Koper, M.T.M. Co-adsorption of Cations as the Cause of the Apparent pH Dependence of Hydrogen Adsorption on a Stepped Platinum Single-Crystal Electrode. *Angew. Chem. Int. Ed.* **2017**, *56*, 15025–15029. [[CrossRef](#)] [[PubMed](#)]
73. Wang, J.; Gao, Y.; Kong, H.; Kim, J.; Choi, S.; Ciucci, F.; Hao, Y.; Yang, S.; Shao, Z.; Lim, J. Non-precious-metal catalysts for alkaline water electrolysis: Operando characterizations, theoretical calculations, and recent advances. *Chem. Soc. Rev.* **2020**, *49*, 9154–9196. [[CrossRef](#)] [[PubMed](#)]